

Hierarchical CuCo Carbonate Hydroxide Nanowires@FeCo-Layered Double Hydroxide Hexagonal Nanosheets of Penetrating Architecture for High-Performance Asymmetric Supercapacitor

Ang Li,^[a] Mei Yi,^[a] Shuimiao Zhao,^[a] Mingxing Luan,^[a] and Jingbo Hu^{*[a, b]}

Rational construction of heterostructures can compensate for the property shortfalls of a single component, which is a promising and challenging approach to develop high-performance electrode materials. Herein, CuCo carbonate hydroxide nanowires@FeCo-layered double hydroxide hexagonal nanosheets (CuCo-CH@FeCo-LDH) with a unique nanowire-penetrated-nanosheet architecture have been prepared through a facile two-step hydrothermal method. The nanowires serve as fast channels for charge transfer of FeCo-LDH and alleviate the blocked electroactive utilization induced by self-stacking of LDH

nanosheets, while the FeCo-LDH contributes high specific capacitance. The resultant CuCo-CH@FeCo-LDH exhibits pseudocapacitive behavior with near-rectangular CV profiles and overall enhanced electrochemical performance compared to individual CuCo-CH and FeCo-LDH. An assembled asymmetric supercapacitor (CuCo-CH@FeCo-LDH//N/S co-doped graphene) delivers high energy density (46.9 Wh kg⁻¹ at 750 W kg⁻¹), high power density (29.0 Wh kg⁻¹ at 7500 W kg⁻¹), and outstanding cycling stability (81.7% capacitance retention after 5000 cycles).

Introduction

With the scarcity of fossil energy and the increasingly serious environmental problems, the development of high-performance functional materials and devices for energy conversion and storage has become particularly urgent.^[1–3] Among the various energy storage devices, supercapacitors have attracted widespread attention due to their high power density, ultra-long lifespan and fast charging capability.^[4,5] However, the lower energy density compared to lithium batteries and fuel cells remains a major obstacle to the further application of supercapacitors, and the key to enhancing the energy density of supercapacitors lies in the development of electrode materials with prominent electrochemical properties.^[6–9] According to the way of energy storage, supercapacitors can be divided into electric double layer capacitors and Faraday pseudocapacitors. In contrast to carbon-based electric double layer capacitors with energy storage derived from adsorption-desorption of electrolyte ions on the electrode surface, pseudocapacitors can deliver higher energy density based on

their rapid and reversible surface faradic redox reactions.^[10–12] Hence, great efforts have been endeavored to explore new pseudocapacitive materials with favorable structures allowing exceptional electrochemical performance.

Typically, transition metal layered double hydroxides (LDHs) are an attractive class of potential faradic electrode materials owing to their high theoretical specific capacitance/capacity, unique 2D layered crystal structure, tunable chemical composition, and robust stability in alkaline environment.^[13–18] However, the poor conductivity and easily restacking tendency of LDHs impede their charge transfer and surface reactions, resulting in poor rate capability and a measured specific capacitance/capacity far below the theoretical one.^[19–22] To address the issue of self-stacking, another electrode material is usually introduced to form a mixed structure.^[23–26] As for conductivity, the fact that the typical anisotropic crystal structure of LDHs will produce a clearly anisotropic charge transfer behavior, with superior in-plane hydroxide ion conductivity (10^{-1} S cm⁻¹) but inferior cross-plane hydroxide ion conductivity four to five orders of magnitude lower than the in-plane one.^[27] Furthermore, cobalt can be introduced into the crystal layers of LDHs, which can boost the in-plane electronic conductivity, as Co²⁺ can be oxidized to conductive CoOOH (12.8 S cm⁻¹) during redox reactions.^[13,28] Therefore, the key to raising the overall conductivity of LDHs is to fasten the cross-plane charge transfer, which requires the construction of additional charge transfer channels across the layers of LDHs through the rationally designed architecture.

Basic carbonates with divalent metal ions are common industrial raw materials and widespread in nature.^[29–30] They are usually used as precursors for the synthesis of metal oxides/hydroxides,^[31,32] but their electrochemical performance as

[a] A. Li, M. Yi, S. Zhao, M. Luan, Prof. J. Hu

College of Chemistry
Beijing Normal University
100875 Beijing, P. R. China
E-mail: hujingbo@bnu.edu.cn

[b] Prof. J. Hu

Department of Chemistry
College of Arts and Sciences
Beijing Normal University at Zhuhai
519087 Zhuhai City, Guangdong Province, P. R. China
E-mail: hujingbo@bnu.edu.cn

 Supporting information for this article is available on the WWW under
<https://doi.org/10.1002/batt.202200026>

electrode materials for supercapacitors has received relatively low attention. Basic cobalt carbonate possesses a unique one-dimensional tunnel-like crystal structure, which allows the hydrothermally synthesized crystals to generally exhibit a morphology of nanowire. In contrast to LDHs, the infinite crystal tunnels and nanowire morphology of basic cobalt carbonate facilitate electrolyte to penetrate into the interior, while the CO_3^{2-} attached between the tunnel-like structures provides strong hydrophilicity,^[30,33] and these attributes accommodate the rapid ion transport. In addition, the presence of cobalt ions can also accelerate the electron transfer of basic cobalt carbonate during charging and discharging. Consequently, basic cobalt carbonate nanowires can be ideal channels for rapid charge transfer. Nevertheless, due to the presence of electrochemical inactive carbonate ions, the gravimetric capacitance/capacity of basic cobalt carbonate is lower than that of LDHs. Although doping copper into basic cobalt carbonate to form bimetallic compounds can indeed enrich redox reactions and improve cycling stability,^[34,35] its specific capacitance/capacity is still limited by the chemical composition (a large proportion of inactive CO_3^{2-}).

In this work, we designed and fabricated an architecture of CuCo carbonate hydroxide (CuCo-CH) nanowires penetrating FeCo-LDH hexagonal nanosheets through a facile two-step hydrothermal method. This special architecture is different from the core-shell structure of LDH-encapsulated nanowires reported in most literatures.^[36-39] The nanowires penetrating the FeCo-LDH nanosheets not only act as fast channels for charge transfer to directly compensate for the inherent low cross-plane conductivity of LDH, but also prevent the aggregation of LDH. Benefiting from the rational penetrating structure and the synergistic effect between two components, the resultant pseudocapacitive CuCo-CH@FeCo-LDH electrode delivers large specific capacitance (1206 F g^{-1} at 1 A g^{-1}) with

enhanced rate performance (68% capacitance retention at 10 A g^{-1}) and exhibits ultralong lifespan (83.0% retention after 5000 cycles at 15 A g^{-1}). To achieve both desirable energy density and power density, an asymmetric supercapacitor (ASC) is assembled with the CuCo-CH@FeCo-LDH as positive electrode and N/S co-doped graphene (NSrGO) as negative electrode. The as-prepared ASC exhibits outstanding energy density (46.9 Wh kg^{-1} at 750 W kg^{-1}) and power density (29.0 Wh kg^{-1} at 7500 W kg^{-1}) with steady cycling performance (81.7% retention after 5000 cycles at 10 A g^{-1}).

Results and Discussion

Figure 1 shows the schematic for fabricating of CuCo-CH@FeCo-LDH with penetrating architecture and N/S co-doped graphene. In the first-step hydrothermal reaction, the dissociated Cu^{2+} and Co^{2+} will combine with OH^- and CO_3^{2-} slowly released from the hydrolysis of urea to form CuCo-CH crystalline grains. Some of the grains will then adhere to the NF framework and grow along a specific crystal plane to aggregate into nanowires. Additionally, NH_4F can act as an assistant to activate the substrate to produce more active sites for nucleation and enhance the adhesion between the substrate and the electrochemical active materials.^[40-42] In the second-step hydrothermal reaction, the synthesized CuCo carbonate hydroxide nanowires act as the skeleton to provide nucleation sites for the further growth of FeCo-LDH hexagonal nanosheets and ultimately result a unique nanowire-penetrated-nanosheet architecture of CuCo-CH@FeCo-LDH. Besides, Citrate can effectively chelate and cross-link metal ions, so as to slow down the growth rate of LDH and avoid the aggregation of LDH nanosheets caused by excessive growth. As depicted in Figure S1, an obvious color change from original gray (bare NF,

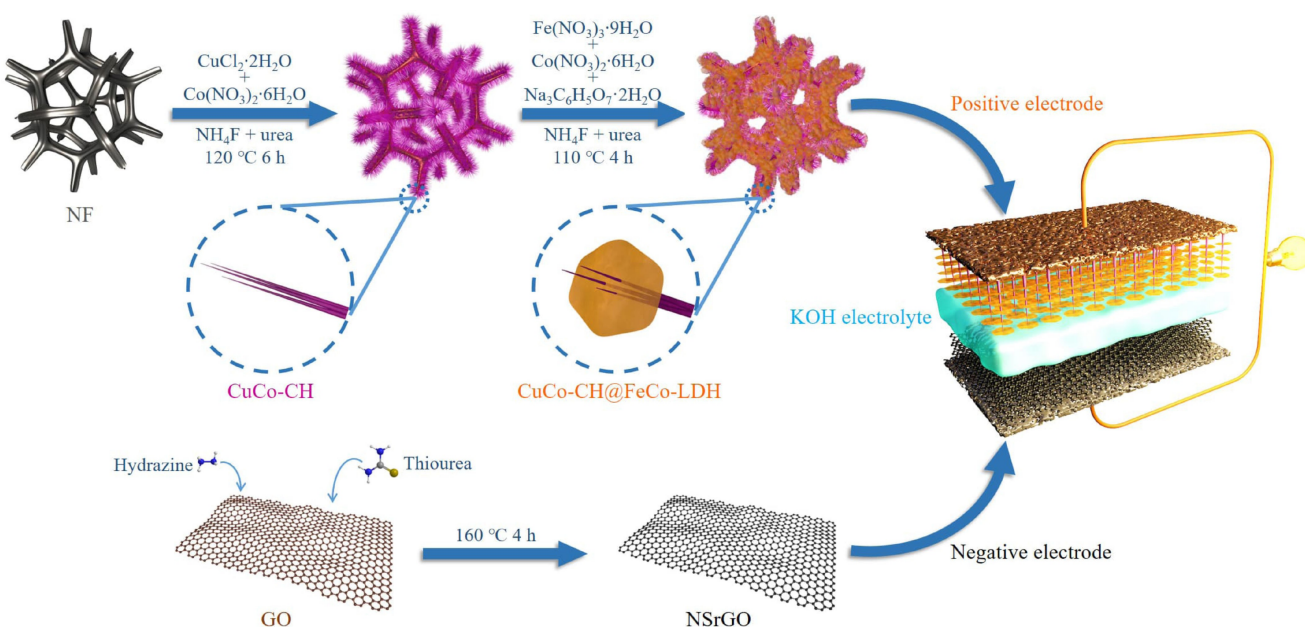


Figure 1. Schematic illustration of the fabricating process for an asymmetric supercapacitor (ASC) based on CuCo-CH@FeCo-LDH and NSrGO.

left) to purple (CuCo-CH, middle), and finally to brown (CuCo-CH@FeCo-LDH, right) was observed during the two-step hydrothermal reaction.

The surface morphologies and microstructures of the as-obtained electrodes were investigated by FE-SEM. As shown in Figures 2(a) and S2(a), the CuCo carbonate hydroxide (CuCo-CH) nanowires are uniformly and completely grown on the NF framework to form a nanowire array with plenty of open free space, which is considered as a charge transfer-favored support. Figure 2(b) depicts that the individual FeCo-LDH structure consists of numerous interconnected nanosheets and is densely deposited on the NF substrate. From the low magnification FE-SEM image of pristine FeCo-LDH (Figure S2b), it can be clearly seen that the nanosheets are accompanied by severe self-stacking, which will hinder the efficient utilization of FeCo-LDH and restrict the charge transfer. For the CuCo-CH@FeCo-LDH heterostructure synthesized at moderate reactant concentrations (Figure 2c,e), it is obvious that the well-crystallized FeCo-LDH hexagonal nanosheets with a diameter of about 2.5 μm are penetrated by CuCo carbonate hydroxide nanowires. As shown in Figure S2(d), no obvious aggregation is observed in CuCo-CH@FeCo-LDH, such a rational-designed penetrating structure can not only enhance the interface coupling between two components, but also prevent the severe self-stacking of FeCo-LDH, which will lead to overall enhanced electrochemical properties. The morphologies of CuCo-CH@FeCo-LDH-1 synthesized at lower reactant concentrations and CuCo-CH@FeCo-LDH-2 synthesized at higher reactant concentrations are displayed in Figure 2(d and f), both samples have a structure of nanowires penetrating nanosheets, but the lower concentrations result in smaller ($\sim 1 \mu\text{m}$ in diameter) nanosheets while the higher concentrations result in larger ($\sim 4 \mu\text{m}$ in diameter) nanosheets. Moreover, non-ignorable accumulations are observed in CuCo-CH@FeCo-LDH-2 (Figure S2e).

Figure 3a displays the XRD patterns of as-obtained FeCo-LDH, CuCo-CH, and CuCo-CH@FeCo-LDH. The active materials were detached from the NF substrate to analyze the crystalline structure for preventing interference caused by the strong peaks of NF. All the diffraction peaks of CuCo-CH could be indexed to crystalline cobalt carbonate hydroxide hydrate (JCPDS no. 48-0083), the weak shift of the XRD diffraction position is a result of doping of copper ions. In the XRD pattern of CuCo-CH@FeCo-LDH, except diffraction peaks from cobalt carbonate hydroxide hydrate, the peaks at 2θ values of 11.7° , 23.4° and 58.9° are corresponding to (003), (006) and (110) planes of hexagonal FeCo-LDH (JCPDS no. 50-0235). Projections of the crystal structure of cobalt carbonate hydroxide along the c and b axis show tunnels surrounded by rings of nine $[\text{CoO}_6]$ octahedrons, and the tunnel structure may play a significant role in fostering the electrolyte penetration into the interior. Obviously, the unsatisfied interlaminar conduction of 2D LDH will lead to poor charge transfer. Significantly, as for CuCo-CH@FeCo-LDH, the penetration of CuCo-CH nanowires can enhance the cross-plane conduction and alleviate the interlayer restacking, which could provide fast channels for charge transfer and more exposed active surface for Faradaic reactions.

XPS analysis further investigates the element valence information of CuCo-CH@FeCo-LDH (Figure 3b–e). The Co 2p spectrum (Figure 3b) is deconvoluted into two strong peaks at 797.6 eV and 781.6 eV assigned to $\text{Co } 2p_{1/2}$ and $\text{Co } 2p_{3/2}$ signals of Co^{2+} .^[43] As shown in Figure 3(c), the Cu 2p spectrum contains two spin-orbit doublets accompanied with two shake-up satellites. The peaks at 932.9 eV and 952.7 eV with a standard split of 19.8 eV generally demonstrate the presence of Cu^+ , whereas the peaks with binding energies at 935.3 and 955.4 eV correspond to Cu^{2+} .^[25] The larger signal noise in the Cu 2p spectrum may be caused by the outer FeCo-LDH nanosheets masking the CuCo-CH nanowires. Figure 3d presents the Fe 2p

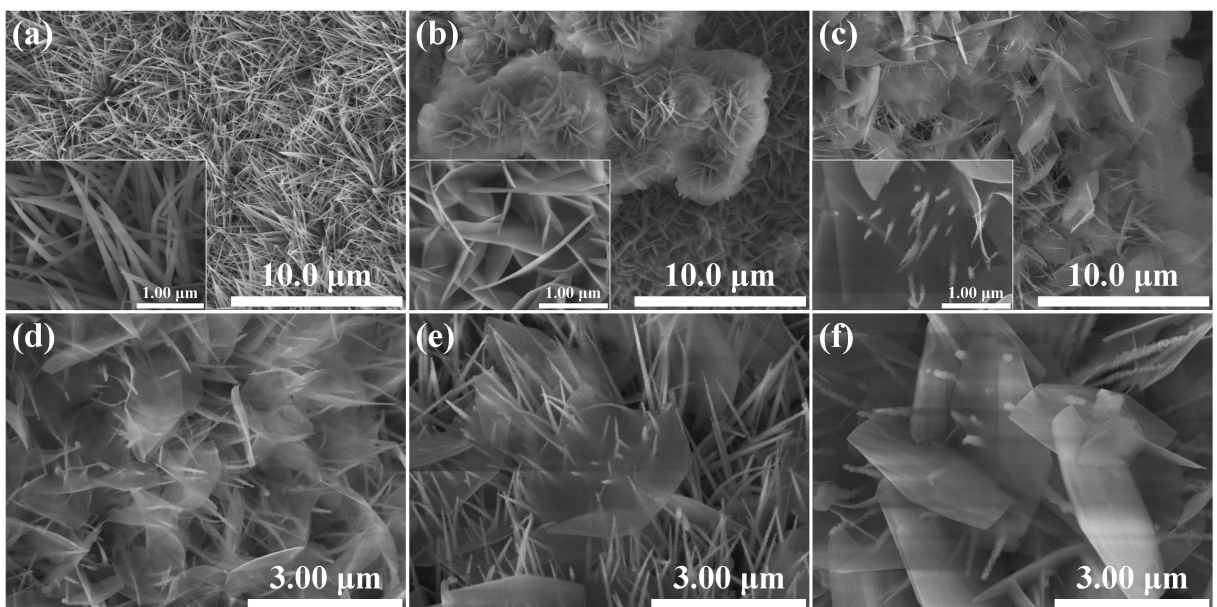


Figure 2. FE-SEM images of a) CuCo-CH, b) FeCo-LDH, c,e) CuCo-CH@FeCo-LDH, d) CuCo-CH@FeCo-LDH-1, f) CuCo-CH@FeCo-LDH-2.

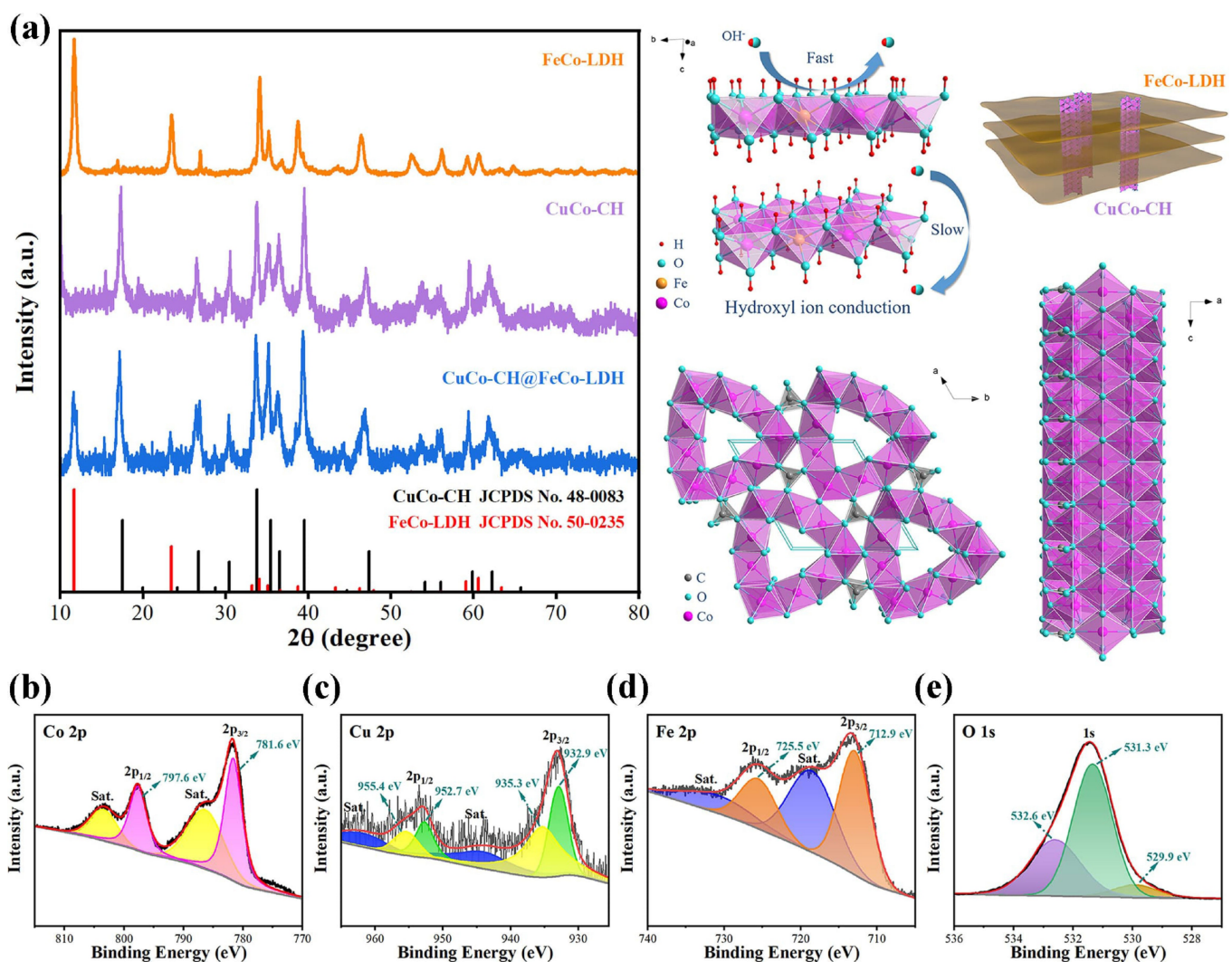


Figure 3. a) XRD patterns of FeCo-LDH, CuCo-CH, and CuCo-CH@FeCo-LDH. The schematic illustration for the anisotropic ion-conducting scenarios of LDH nanosheets, the crystal structure of cobalt carbonate hydroxide, and the heterostructure of CuCo-CH@FeCo-LDH. XPS spectra of b) Co 2p, c) Cu 2p, d) Fe 2p, and e) O 1s for the CuCo-CH@FeCo-LDH.

spectrum in which two main peaks located at 712.9 eV for Fe $2p_{3/2}$ and 725.5 eV for Fe $2p_{1/2}$ accompanied by two satellites at 718.5 and 730.8 eV. Typically, the appearance of satellite bands near the Fe 2p main peaks is considered to be an indicator of Fe^{3+} valence state.^[44] In the O 1s spectrum (Figure 3e), the strongest peak at 531.3 eV is commonly assigned to metal-hydroxyl group, the medium peak at 532.6 eV could be indexed to physically or chemically adsorbed water, and the weakest peak at 529.9 eV is associated with metal-oxygen bond derived from a small amount of metal oxides formed on the surface due to the loss of water from LDH.^[45]

Detailed structural information of CuCo-CH@FeCo-LDH was further investigated by TEM. Figure 4(a) shows CuCo-CH nanowires with an average diameter of about 60 nm combined with FeCo-LDH hexagonal nanosheets. The electron beam can penetrate ultrathin samples, which allows the FeCo-LDH hexagonal nanosheets to be semitransparent under TEM observation. The thickness was measured quantitatively by atomic force microscope to be about 4 nm (Figure S3). It is

noteworthy that there are also some small nanosheets with irregular shapes on the nanowires. The characterization results of SAED and EDS (Figure S4) show that the small nanosheets are amorphous and mainly composed of Fe element, which may be FeOOH formed by Fe^{3+} hydrolysis. The HRTEM image (Figure 4b) captured at the interface between a nanowire and a hexagonal nanosheet exhibits interplanar spacings of the (100) lattice planes of CuCo carbonate hydroxide with 0.872 nm and (101) lattice planes of FeCo-LDH with 0.268 nm, respectively. Moreover, it is obvious that the growth direction of CuCo-CH nanowires is parallel to the [100] direction, which is similar to that of previous reports.^[32,46] The corresponding SAED patterns of this heterostructure reveal the single-crystalline feature of both CuCo-CH and FeCo-LDH. Figure 4(c) shows the elemental mapping of CuCo-CH@FeCo-LDH. It is clear that the signal of Fe is primarily distributed in the nanosheet region, whereas Cu elements are dominant in the nanowire region, further confirming the heterostructure of CuCo-CH nanowires@ FeCo-LDH hexagonal nanosheets.

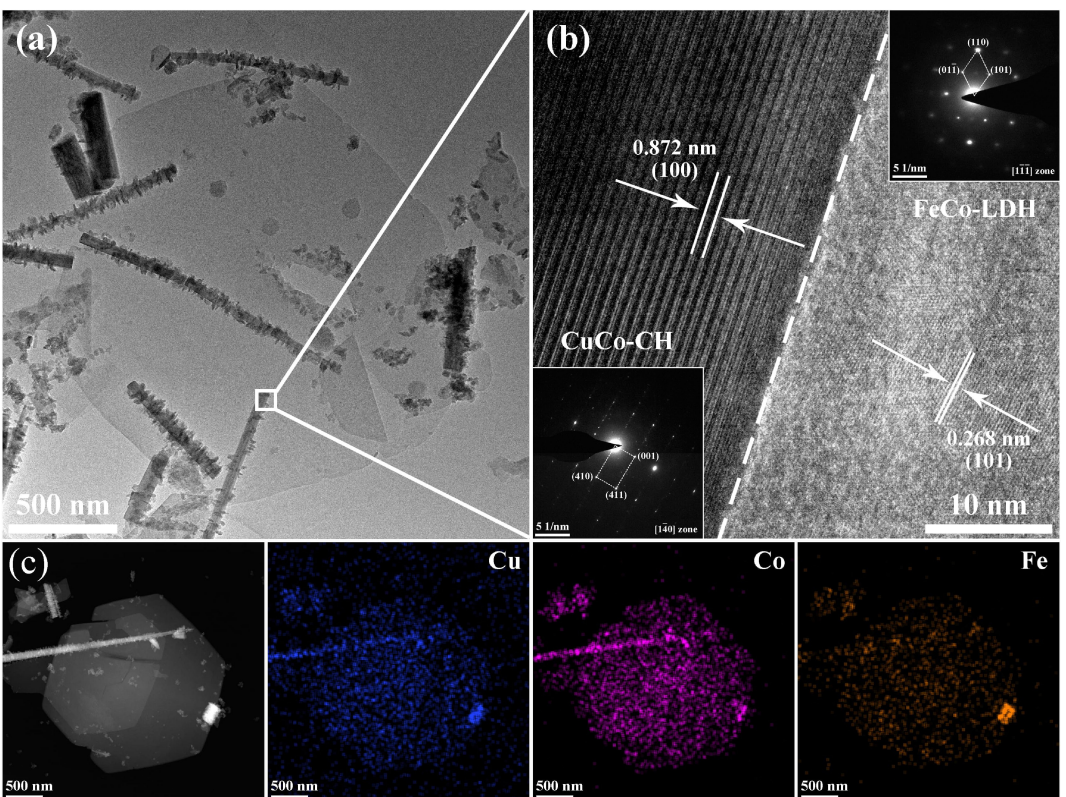


Figure 4. a) TEM image and b) HRTEM image of CuCo-CH@FeCo-LDH, the insets show the corresponding SAED patterns. c) STEM image and elemental mapping of CuCo-CH@FeCo-LDH.

The electrochemical properties of the synthesized electrodes were examined by cyclic voltammetry (CV), galvanostatic charge/discharge (GCD), and electrochemical impedance spectroscopy (EIS) analysis in a three-electrode configuration. Figure 5(a) displays CV curves of the CuCo-CH@FeCo-LDH electrode at different scan rates in the potential window of 0 to 0.5 V. Intriguingly, unlike most metal compounds with distinct paired redox peaks, the CV profile of this electrode exhibits a near-rectangular shape, which is more similar to that of most electrical double-layer carbonaceous materials. In addition, all the CV profiles are maintained with no obvious deviation as the scan rate increases from 10 to 50 mVs⁻¹, implying high electrochemical reversibility of the CuCo-CH@FeCo-LDH electrode. To further explore the electrochemical reaction kinetic behaviors of this electrode, the CV curves were used to evaluate the quantitative comparisons between diffusion-controlled process and surface capacitive process according to the following relationship:^[47]

$$i(V) = k_1 v + k_2 v^{1/2} \quad (1)$$

where $i(V)$ refers to the total current density at a fixed potential V , v is the scan rate, $k_1 v$ and $k_2 v^{1/2}$ respectively represent the current density contributed by surface capacitive process and diffusion-controlled process. Figure S5 depicts the calculated decoupling results of CuCo-CH@FeCo-LDH at different scan rates, the shaded regions indicate the capacitive

contributions, while the unshaded regions represent the diffusion-controlled contributions. The percentage contributions of capacitive process at scan rates from 10 to 50 mVs⁻¹ are summarized in a histogram (Figure 5b). From the kinetic analysis, it can be inferred that the approximately rectangular cyclic voltammetry curves of the CuCo-CH@FeCo-LDH do not come from the highly dispersed electroactive materials, which may shorten the diffusion length and fasten the diffusion-controlled reaction into a surface kinetic reaction process similar to the nano-sized LiCo₂O₄,^[48] since the diffusion-controlled process still contributes for a high proportion, especially at slow scan rate. These near-rectangular CV profiles are more likely from the overlap of successive redox reaction peaks of different metal ions, and these reactions are still dominated by diffusion control. CV measurements of CuCo-CH, FeCo-LDH, CuCo-CH@FeCo-LDH-1, and CuCo-CH@FeCo-LDH-2 at scan rates ranged from 10 to 50 mVs⁻¹ are displayed in Figure S6(a-d). The CV curves of pristine CuCo-CH and FeCo-LDH show a pair of typical redox peaks, implying the characteristics of battery-type electrodes. In contrast, CuCo-CH@FeCo-LDH-1 and CuCo-CH@FeCo-LDH-2 exhibit distorted rectangular CV profiles, which are more like pseudocapacitive electrodes.

Figure 5(c) shows the GCD curves of CuCo-CH@FeCo-LDH at current densities from 1 to 10 Ag⁻¹ within a potential range of 0 to 0.45 V. The roughly symmetric shapes of all the GCD curves indicate desirable coulombic efficiency, while the near-triangular profiles correspond to the near-rectangular CV curves. The

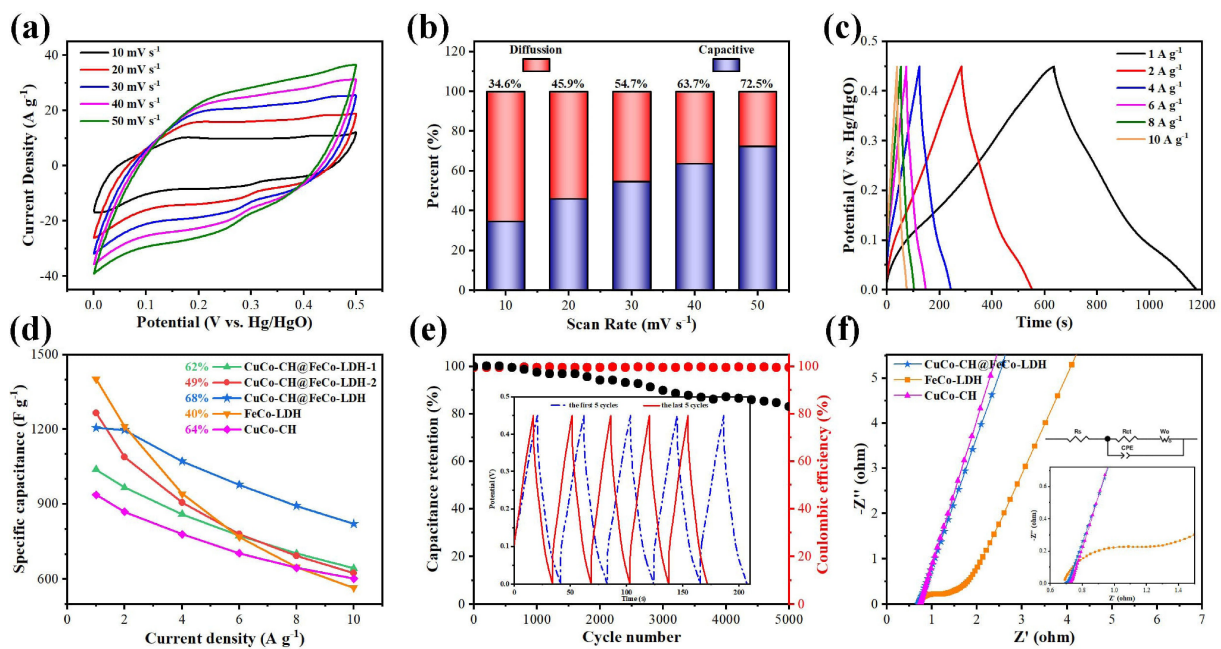


Figure 5. a) CV curves of CuCo-CH@FeCo-LDH at different scan rates. b) Capacitive contribution ratio at different scan rates of CuCo-CH@FeCo-LDH. c) GCD curves of CuCo-CH@FeCo-LDH at different current densities. d) Specific capacitance as a function of current density. e) Capacitance retention and Coulombic efficiency over 5000 cycles at 15 A g⁻¹ (the inset shows the first and last 5 GCD curves). f) Nyquist plots recorded in a frequency range from 0.01 Hz to 100 kHz.

GCD curves of CuCo-CH, FeCo-LDH, CuCo-CH@FeCo-LDH-1, and CuCo-CH@FeCo-LDH-2 tested at different current densities are depicted in Figure S7(a-d). The specific capacitance values of as-prepared electrodes at different current densities are calculated from the corresponding GCD curves, and the results are shown in Figure 5(d). It can be found that the pristine FeCo-LDH electrode possesses the largest specific capacitance of 1402 F g⁻¹ at a low current density of 1 A g⁻¹ but the least ideal rate capability with only 40% capacitance retention at 10 A g⁻¹. Meanwhile, as a comparison, the individual CuCo-CH electrode achieves desirable retention rate of 64% from 1 to 10 A g⁻¹, but the specific capacitance is unsatisfied. Combining the advantages of both components, the CuCo-CH@FeCo-LDH electrode exhibits specific capacitance values of 1206, 1197, 1071, 977, 892, and 821 F g⁻¹ at the corresponding current densities of 1, 2, 4, 6, 8 and 10 A g⁻¹, demonstrating overall enhanced energy-storage performance and rate capability (68% retention). Insufficient loading of FeCo-LDH and agglomeration caused by excessive loading lead to inferior specific capacitance of the CuCo-CH@FeCo-LDH-1 electrode and poor rate performance of the CuCo-CH@FeCo-LDH-2 electrode, respectively, which suggest the CuCo-CH@FeCo-LDH electrode is the optimized one.

The cyclic performance of the CuCo-CH@FeCo-LDH electrode was evaluated by repeated charge/discharge for 5000 cycles at a current density of 15 A g⁻¹. As illustrated in Figures 5(e) and S8, the CuCo-CH@FeCo-LDH electrode displays steady cycling stability with 83.0% retention of the initial capacitance, which is comparable to the pristine CuCo-CH electrode (89.9% retention after 5000 cycles) and superior to the individual FeCo-LDH electrode (72.0% retention after 5000 cycles). The inset of Figure 5e shows the first and last 5 GCD traces of CuCo-CH@FeCo-LDH. Notably, the inconspicuous

shape change of GCD curves after durability test signifies exceptional stability. Additionally, the coulomb efficiency is kept at almost 100% throughout all 5000 cycles. The SEM images after 5000 charge-discharge cycles are presented in Figure S9. It is found that the morphology of pristine CuCo-CH transforms from nanowires to nanoribbons. According to a previous report,^[49] this change is attributed to the phase transition of CuCo carbonate hydroxide to CuCo-LDH during charge-discharge process. The CuCo-CH@FeCo-LDH after durability test exhibits the structure of hexagonal nanosheets connected by interlaced nanoribbons without agglomeration and collapse as in the case of individual FeCo-LDH, verifying its remarkable cycling stability.

The conductivity behavior of the as-obtained electrodes was revealed by EIS measurements and the Nyquist plots with the corresponding equivalent circuit are presented in Figure 5(f). The real axis intercept indicates the solution resistance (R_s), which is mainly contributed by the ionic resistance of the electrolyte. The nearly equivalent R_s values for these three electrodes stem from the same electrolyte and test environment. The diameter of the semicircle in high-frequency region corresponds to the charge transfer resistance (R_{ct}). Impressively, the mixed CuCo-CH@FeCo-LDH shows an R_{ct} value almost equal to that of individual CuCo-CH and far smaller than that of individual FeCo-LDH, which validate the rational design of nanowire-penetrated-nanosheet architecture can indeed boost the electrical conductivity and charge-transfer kinetics.

As for the negative electrode, the NSrGO was examined by FE-SEM and TEM-EDS before assembling the ASC device. As shown in Figure S10(a), the NSrGO displays a morphology of ultrathin nanosheets with wrinkles and curly edges. Elemental mapping (Figure S10b and c) shows uniform distribution of

element C, O, N and S in NSrGO. The individual electrochemical properties of NSrGO in a three-electrode system were also investigated. Figures S11(a) and Figure S12 show the CV curves and the capacitive contribution ratio of NSrGO at different scan rates, respectively. All CV curves exhibit large capacitive contribution and near rectangular shape, suggesting the major kinetic behaviors of an electrical double-layer capacitor (EDLC). As shown in Figure S11(b), the almost symmetric GCD curves at different current densities illustrate the favorable electrochemical reversibility of the NSrGO electrode. The NSrGO delivers a specific capacitance of 338 F g^{-1} at 1 A g^{-1} calculated from the corresponding GCD curve. When the current density is increased to 10 A g^{-1} , this electrode still keeps 73% of the capacitance retention, demonstrating outstanding rate performance. Like most typical carbonaceous materials, NSrGO is endowed with superior cycling stability with only 4.7% of capacitance decays after 5000 cycles at 15 A g^{-1} (Figure S11d).

Afterwards, an alkaline ASC device was assembled employing CuCo-CH@FeCo-LDH as positive electrode and NSrGO as negative electrode. Figure 6(a) shows the CV curves of CuCo-CH@FeCo-LDH and NSrGO, suggesting the ASC could reach a safe operating potential of about 1.5 V. The CV curves of the as-fabricated ASC measured in various potential window at a scan rate of 10 mV s^{-1} are depicted in Figure 6b. In the potential range of 1.1 to 1.4 V, the CV curves display inadequate capacity areas with incomplete redox peaks, which is due to the insufficient redox reactions of the pseudocapacitive positive electrode. When the working potential reaches 1.5 V, all redox peaks appear. As shown in the CV curve of 1.6 V, higher working voltage will induce oxygen evolution reaction on the

electrode surface, resulting in significant polarization current. Hence, the optimal working potential is determined to be 1.5 V. Figure 6(c) displays the CV profiles of the CuCo-CH@FeCo-LDH//NSrGO ASC examined at the optimal working potential range of 0 to 1.5 V with different scan rates. As the scan rate increases, the shapes of the CV curves stay almost invariable, demonstrating fast redox rate and excellent rate capability.

GCD curves with different operating potential from 1.1 to 1.6 V at a current density of 1 A g^{-1} are illustrated in Figure 6d. The discharge time prolongs with the increasing voltage window and all GCD curves are approximately symmetric without overcharge, further confirming the optimal voltage window of 1.5 V. The GCD curves and the corresponding specific capacitance values of the ASC at different current densities are shown in Figure S13a and Figure S13(b), respectively. The resultant specific capacitance values are calculated to be 150, 137, 120, 110, 101, 93 F g^{-1} at $1, 2, 4, 6, 8, 10 \text{ A g}^{-1}$, and the retention rate is 62% from 1 to 10 A g^{-1} , implying outstanding rate capability. The cyclic performance of the ASC device is evaluated by continuous charge/discharge test at 10 A g^{-1} . The ASC displays ultralong lifespan with 81.7% retention of the initial capacitance after 5000 cycles. Furthermore, the coulombic efficiency remains nearly 100% throughout all the process. Ragone plots illustrate the relation between energy density and power density. As shown in Figure 6(f), the as-assembled ASC provides a prominent energy density of 46.9 Wh kg^{-1} at 750 W kg^{-1} . Even when the power density expands tenfold to 7500 W kg^{-1} , the energy density still remains at 29.0 Wh kg^{-1} . Notably, the energy storage performance of the as-fabricated CuCo-CH@FeCo-LDH//NSrGO ASC exceeds

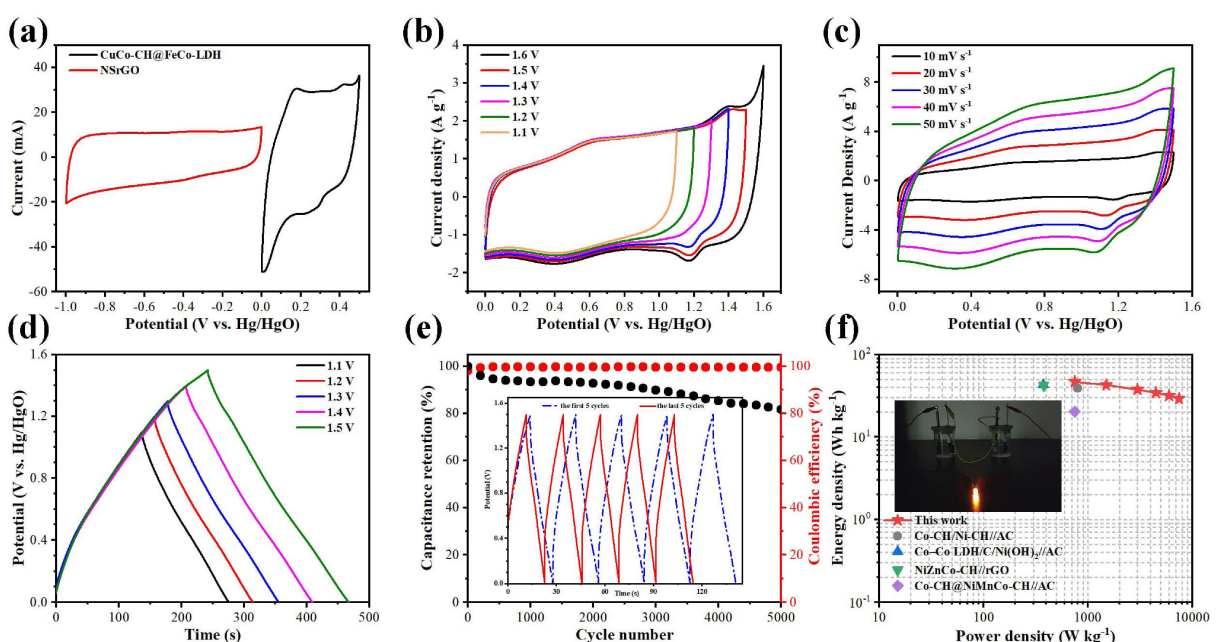


Figure 6. a) Comparison CV curves of CuCo-CH@FeCo-LDH and NSrGO electrodes at 10 mV s^{-1} . b) CV curves of the CuCo-CH@FeCo-LDH//NSrGO ASC with different operating voltage windows at 10 mV s^{-1} . c) CV curves with a potential range from 0 to 1.5 V recorded at different scan rates. d) GCD curves of the ASC with different operating voltage windows at 1 A g^{-1} . e) Capacitance retention and coulombic efficiency over 5000 cycles at 10 A g^{-1} (the inset shows the first and last 5 GCD curves). f) Ragone plots of the CuCo-CH@FeCo-LDH//NSrGO ASC in comparison to relevant ASC (the inset shows a glowing LED with two series-connected ASC devices).

that of most similar devices in previous reports, such as Co-CH/Ni-CH//AC (39.2 Wh kg⁻¹ at 800 W kg⁻¹),^[30] Co-Co LDH/C/Ni-(OH)₂//AC (42.9 Wh kg⁻¹ at 375 W kg⁻¹),^[50] NiZnCo-CH//rGO (42.3 Wh kg⁻¹ at 376 W kg⁻¹),^[51] and Co-CH@NiMnCo-CH//AC (20.3 Wh kg⁻¹ at 748 W kg⁻¹).^[52] Lastly, a yellow LED was lighted by two ASC devices in series (Figures 6f and S14).

Conclusion

In summary, CuCo carbonate hydroxide nanowires@FeCo-layered double hydroxide hexagonal nanosheets have been successfully prepared via a facile two-step hydrothermal method. Owing to the rationally designed nanowire-penetrated-nanosheet architecture in which CuCo-CH nanowires act as fast channels for charge transfer to directly compensate for the intrinsic poor cross-plane conductivity of LDH and alleviate the interlaminar restacking, the CuCo-CH@FeCo-LDH electrode presents desirable specific capacitance of 1206 F g⁻¹ at 1 A g⁻¹ with enhanced rate performance (68% capacitance retention at 10 A g⁻¹), and exceptional cycling stability (83.0% capacitance retention after 5000 cycles at 15 A g⁻¹). Additionally, the assembled CuCo-CH@FeCo-LDH//NSrGO ASC device provides a prominent energy density (46.9 Wh kg⁻¹ at 750 W kg⁻¹), an extraordinary power density (29.0 Wh kg⁻¹ at 7500 W kg⁻¹), and ultralong lifespan (81.7% capacitance retention after 5000 cycles at 10 A g⁻¹). Therefore, the above results suggest that CuCo-CH@FeCo-LDH would be a promising electrode material for high-performance supercapacitors and our design concept may offer a potential strategy to develop other advanced electrode materials with similar microstructures.

Experimental Section

Synthesis of CuCo carbonate hydroxide nanowires

All chemical reagents were of analytical grade and directly used without further purification. Before reaction, nickel foam (30 mg cm⁻², 0.5 mm in thickness) was ultrasonically cleaned with HCl (3 M), acetone and triple-distilled water for 15 min each, then dried at 60 °C. Firstly, CuCl₂·2H₂O (0.7 mmol), Co(NO₃)₂·6H₂O (1.05 mmol), NH₄F (3.0 mmol) and urea (5.0 mmol) were dissolved in 35 mL triple-distilled water to obtain a homogeneous light purple solution. Afterwards, the solution was poured into a 50 mL PTFE-lined stainless steel autoclave, and a piece of pre-treated nickel foam (1×4 cm) fixed with a holder was placed perpendicularly staying in. The autoclave was then sealed for a hydrothermal reaction at 120 °C for 6 h, and naturally cooled down to ambient temperature. Finally, the nickel foam (NF) with anchored purple CuCo carbonate hydroxide (CuCo-CH) nanowires was washed several times using triple-distilled water and ethanol followed by drying at 60 °C. The mass loading of CuCo carbonate hydroxide was ~1.3 mg cm⁻².

Synthesis of CuCo carbonate hydroxide nanowires@FeCo-LDH hexagonal nanosheets

Typically, 0.3 mmol of Fe(NO₃)₃·9H₂O, 0.6 mmol of Co(NO₃)₂·6H₂O, 1.8 mmol of NH₄F, 1.8 mmol of urea and 4.5 mg of trisodium citrate

dihydrate were dissolved in 30 mL triple-distilled water to form a transparent pink solution. Then the solution was transferred into a 50 mL PTFE-lined stainless steel autoclave and the as-prepared NF loaded with CuCo-CH was vertically placed in. The apparatus was sealed and maintained at 110 °C for 4 h. After the second-step hydrothermal reaction, the resultant CuCo-CH@FeCo-LDH grown on NF was obtained, then rinsed with triple-distilled water and ethanol repeatedly and dried at 60 °C. For comparison, a same hydrothermal reaction with bare NF was simultaneously carried out in the same procedure, and the obtained product was denoted as FeCo-LDH. In addition, Control experiments using lower (2/3 of the above additions) and higher (4/3 of the above additions) reactant concentrations were also performed in the same hydrothermal process while remaining other conditions, and the products obtained under lower concentration and higher concentration were denoted as CuCo-CH@FeCo-LDH-1 and CuCo-CH@FeCo-LDH-2, respectively. The corresponding mass loading of CuCo-CH@FeCo-LDH-1, CuCo-CH@FeCo-LDH, CuCo-CH@FeCo-LDH-2, and FeCo-LDH was approximately 1.4, 1.5, 1.6, and 1.4 mg cm⁻².

Synthesis of N/S co-doped graphene

The graphene oxide (GO) was obtained by a modified Hummers method. 80 mg of dry GO powder and 1.6 g of thiourea were added into 38 mL of triple-distilled water with continuous sonication for 2 h, then 2 mL of hydrazine hydrate was poured in and stirred for 10 min. The dispersion was transferred into a 50 mL PTFE-lined stainless steel autoclave followed by a hydrothermal reaction conducted at 160 °C for 4 h. After cooling down to ambient temperature naturally, the obtained product was washed several times with ethanol and labelled as NSrGO. To prepare NSrGO electrode for electrochemical measurements, 85 wt% of NSrGO, 5 wt% of acetylene black, and 10 wt% of polyvinylidene fluoride (PVDF) were dispersed in an appropriate amount of N-methylpyrrolidene (NMP) by vigorous stirring and sonicating, the as-obtained slurry was pasted on cleaned NF, dried at 60 °C, and then pressed at 1 MPa.

Material characterization

The morphologies and microstructures of the synthesized materials were investigated using a field emission scanning electron microscope (FE-SEM, Hitachi S-8010). Transmission electron microscopy (TEM), high-resolution TEM (HRTEM) images, and selected area electron diffraction (SAED) were collected on a transmission electron microscope (TEM, FEI Talos F200S). Powder XRD data were collected using a Bruker model D8 Advance powder diffractometer equipped with a Cu K α radiation source ($\lambda=1.5418 \text{ \AA}$) at room temperature. X-ray photoelectron spectroscopy (XPS, AXIS-Ultra instrument, Kratos) was carried out to analyze the valence states and chemical compositions. The elemental analysis was also measured by an electron dispersive X-ray spectrometer (EDS) coupled to the TEM.

Electrochemical measurements

The electrochemical performance of a single electrode was measured in 6 M KOH aqueous solution using a CHI 760E electrochemical workstation (Chenhua, Shanghai). In a typical three-electrode system, the as-prepared electrodes were directly served as the working electrode, Hg/HgO and Pt wire as reference electrode and counter electrode, respectively. EIS analysis was performed over a frequency range between 100 kHz and 0.01 Hz, with a 5 mV AC voltage superimposed at the open circuit potential.

The specific capacitance (C_s , F g^{-1}) and the Coulombic efficiency (η) were calculated from GCD curves using the following equations:

$$C_s = \frac{I \times \Delta t}{m \times \Delta V} \quad (2)$$

$$\eta = \frac{t_d}{t_c} \quad (3)$$

where I is the constant discharge current (A), Δt is the discharge time (s), m is the mass of electroactive materials (g), and ΔV represents the operating potential range. t_d and t_c are the discharge time (s) and charge time (s).

Fabrication of asymmetric supercapacitor

An asymmetric supercapacitor (ASC) was assembled using CuCo-CH@FeCo-LDH as the positive electrode, NSrGO as the negative electrode, and KOH (6 M) aqueous solution as the electrolyte. The energy storage capability of the ASC was tested in a two-electrode system. The loading mass ratio between the positive electrode and the negative electrode was balanced according to Equation (4):

$$\frac{m_+}{m_-} = \frac{C_- \times \Delta V_-}{C_+ \times \Delta V_+} \quad (4)$$

Where m is the mass of the electroactive materials on the positive (+) and the negative (-) electrode, C is the specific capacitance, and ΔV represents the voltage window.

The optimal mass ratio was set to ~ 0.61 , and the mass loadings of the positive and negative electrodes were ~ 3.0 mg and ~ 4.9 mg, respectively. The energy density (E , Wh kg^{-1}) and power density (P , W kg^{-1}) of the ASC were measured as follows:

$$E = \frac{C_s \times \Delta V^2}{2 \times 3.6} \quad (5)$$

$$P = \frac{E \times 3600}{t_d} \quad (6)$$

Acknowledgements

This research was supported by the Fundamental Research Funds for the Central Universities and the National Natural Science Foundation of China (Grant No. 21590801).

Conflict of Interest

The authors declare no conflict of interest.

Data Availability Statement

The data that support the findings of this study are available from the corresponding author upon reasonable request.

Keywords: asymmetric supercapacitor • electrochemistry • energy storage • hydrothermal synthesis

- [1] J. R. Miller, P. Simon, *Science* **2008**, *321*, 651–652.
- [2] P. Simon, Y. Gogotsi, B. Dunn, *Science* **2014**, *343*, 1210–1211.
- [3] Y. Wang, Y. Song, Y. Xia, *Chem. Soc. Rev.* **2016**, *45*, 5925–5950.
- [4] M. F. El-Kady, V. Strong, S. Dubin, R. B. Kaner, *Science* **2012**, *335*, 1326–1330.
- [5] P. Huang, C. Lethien, S. Pinaud, K. Brousse, R. Laloo, V. Turq, M. Respaud, A. Demortiere, B. Daffos, P. L. Taberna, B. Chaudret, Y. Gogotsi, P. Simon, *Science* **2016**, *351*, 691–695.
- [6] G. Wang, L. Zhang, J. Zhang, *Chem. Soc. Rev.* **2012**, *41*, 797–828.
- [7] H. Xie, S. Tang, J. Zhu, S. Vonkehr, X. Meng, *J. Mater. Chem. A* **2015**, *3*, 18505–18513.
- [8] C. Guan, Y. Wang, Y. Hu, J. Liu, K. H. Ho, W. Zhao, Z. Fan, Z. Shen, H. Zhang, J. Wang, *J. Mater. Chem. A* **2015**, *3*, 23283–23288.
- [9] Z. Wu, L. Jiang, W. Tian, Y. Wang, Y. Jiang, Q. Gu, L. Hu, *Adv. Energy Mater.* **2019**, *9*.
- [10] X. Yu, S. Yun, J. S. Yeon, P. Bhattacharya, L. Wang, S. W. Lee, X. Hu, H. S. Park, *Adv. Energy Mater.* **2018**, *8*.
- [11] B. Kirubasankar, P. Palanisamy, S. Arunachalam, V. Murugadoss, S. Angaiah, *Chem. Eng. J.* **2019**, *355*, 881–890.
- [12] T. Liu, L. Zhang, B. Cheng, J. Yu, *Adv. Energy Mater.* **2019**, *9*.
- [13] S. D. Liu, S. C. Lee, U. Patil, I. Shackery, S. Kang, K. Zhang, J. H. Park, K. Y. Chung, S. C. Jun, *J. Mater. Chem. A* **2017**, *5*, 1043–1049.
- [14] X. Li, D. Du, Y. Zhang, W. Xing, Q. Xue, Z. Yan, *J. Mater. Chem. A* **2017**, *5*, 15460–15485.
- [15] X. Zheng, H. Quan, X. Li, H. He, Q. Ye, X. Xu, F. Wang, *Nanoscale* **2016**, *8*, 17055–17063.
- [16] P. Bhojane, L. Sinha, U. K. Goutam, P. M. Shirage, *Electrochim. Acta* **2019**, *296*, 112–119.
- [17] A. Seijas-Da Silva, R. Sanchis-Gual, J. A. Carrasco, V. Oestreicher, G. Abellán, E. Coronado, *Batteries & Supercaps* **2020**, *3*, 499–509.
- [18] Z. Pan, Y. Jiang, P. Yang, Z. Wu, W. Tian, L. Liu, Y. Song, Q. Gu, D. Sun, L. Hu, *ACS Nano* **2018**, *12*, 2968–2979.
- [19] R. Patel, J. T. Park, M. Patel, J. K. Dash, E. B. Gowd, R. Karpoormath, A. Mishra, J. Kwak, J. H. Kim, *J. Mater. Chem. A* **2018**, *6*, 12–29.
- [20] M. F. Warsi, I. Shakir, M. Shahid, M. Sarfraz, M. Nadeem, Z. A. Gilani, *Electrochim. Acta* **2014**, *135*, 513–518.
- [21] W. R. Zou, W. X. Guo, X. Y. Liu, Y. L. Luo, Q. L. Ye, X. T. Xu, F. Wang, *Chem. Eur. J.* **2018**, *24*, 19309–19316.
- [22] C. X. Lu, Y. Yan, T. F. Zhai, Y. Z. Fan, W. Zhou, *Batteries & Supercaps* **2020**, *3*, 534–540.
- [23] D. Han, Y. Zhao, Y. Shen, Y. Wei, L. Mao, G. Zeng, *J. Electroanal. Chem.* **2020**, *859*.
- [24] X. Bai, J. Liu, Q. Liu, R. Chen, X. Jing, B. Li, J. Wang, *Chem. Eur. J.* **2017**, *23*, 14839–14847.
- [25] A. Li, M. Zhai, M. Luan, J. Hu, *Chem. Eur. J.* **2021**, *27*, 10134–10141.
- [26] J.-J. Zhou, X. Han, K. Tao, Q. Li, Y.-L. Li, C. Chen, L. Han, *Chem. Eng. J.* **2018**, *354*, 875–884.
- [27] P. Sun, R. Ma, X. Bai, K. Wang, H. Zhu, T. Sasaki, *Sci. Adv.* **2017**, *3*.
- [28] R. Li, Z. Hu, X. Shao, P. Cheng, S. Li, W. Yu, W. Lin, D. Yuan, *Sci. Rep.* **2016**, *6*.
- [29] S. Zhu, Z. D. Wang, F. Z. Huang, H. Zhang, S. K. Li, *J. Mater. Chem. A* **2017**, *5*, 9960–9969.
- [30] G. F. Zhang, P. Qin, R. Nasser, S. K. Li, P. Chen, J. M. Song, *Chem. Eng. J.* **2020**, *387*.
- [31] Y. Ouyang, H. T. Ye, X. F. Xia, X. Y. Jiao, G. M. Li, S. Mutahir, L. Wang, D. Mandl, W. Lei, Q. L. Hao, *J. Mater. Chem. A* **2019**, *7*, 3228–3237.
- [32] X.-h. Xia, J.-p. Tu, Y.-q. Zhang, Y.-j. Mai, X.-l. Wang, C.-d. Gu, X.-b. Zhao, *RSC Adv.* **2012**, *2*, 1835–1841.
- [33] B. He, H. Liu, Z. Lin, L. Yan, J. Ning, Y. Zhong, C. Zheng, Z. Zhang, Y. Hu, *Chem. Eng. J.* **2019**, *359*, 924–932.
- [34] Y. Guo, X. Hong, Y. Wang, Q. Li, J. Meng, R. Dai, X. Liu, L. He, L. Mai, *Adv. Funct. Mater.* **2019**, *29*, 1809004.
- [35] S. H. Guo, P. W. Yuan, J. Wang, W. Q. Chen, K. Y. Ma, F. Liu, J. P. Cheng, *J. Electroanal. Chem.* **2017**, *807*, 10–18.
- [36] X. Han, Y. J. Yang, J. J. Zhou, Q. X. Ma, K. Tao, L. Han, *Chem. Eur. J.* **2018**, *24*, 18106–18114.
- [37] K. K. Sarigamala, S. Shukla, A. Struck, S. Saxena, *Microsyst. Nanoeng.* **2019**, *5*.
- [38] H. Y. Liang, T. S. Lin, S. Y. Wang, H. N. Jia, C. Li, J. Cao, J. C. Feng, W. D. Fei, J. L. Chi, *Dalton Trans.* **2020**, *49*, 196–202.

- [39] C. P. Duan, L. L. Wang, J. P. Liu, Y. N. Qu, J. Gao, Y. Y. Yang, B. Wang, J. H. Li, L. L. Zheng, M. Z. Li, Z. Yin, *ChemElectroChem* **2021**, *8*, 2272–2281.
- [40] Y. Chen, B. Qu, L. Hu, Z. Xu, Q. Li, T. Wang, *Nanoscale* **2013**, *5*, 9812–9820.
- [41] Q. Wang, X. Wang, J. Xu, X. Ouyang, X. Hou, D. Chen, R. Wang, G. Shen, *Nano Energy* **2014**, *8*, 44–51.
- [42] J. Wang, Y. Zhang, J. Ye, H. Wei, J. Hao, J. Mu, S. Zhao, S. Hussain, *RSC Adv.* **2016**, *6*, 70077–70084.
- [43] S. Liu, K. S. Hui, K. N. Hui, V. V. Jadhav, Q. X. Xia, J. M. Yun, Y. R. Cho, R. S. Mane, K. H. Kim, *Electrochim. Acta* **2016**, *188*, 898–908.
- [44] R. Z. Ma, J. B. Liang, K. Takada, T. Sasaki, *J. Am. Chem. Soc.* **2011**, *133*, 613–620.
- [45] X. Y. He, R. M. Li, J. Y. Liu, Q. Liu, R. R. Chen, D. L. Song, J. Wang, *Chem. Eng. J.* **2018**, *334*, 1573–1583.
- [46] S. Xiong, J. S. Chen, X. W. Lou, H. C. Zeng, *Adv. Funct. Mater.* **2012**, *22*, 861–871.
- [47] T. Brezesinski, J. Wang, S. H. Tolbert, B. Dunn, *Nat. Mater.* **2010**, *9*, 146–151.
- [48] V. Augustyn, P. Simon, B. Dunn, *Energy Environ. Sci.* **2014**, *7*, 1597–1614.
- [49] S. Li, Y. Zhang, N. Liu, C. Yu, S.-J. Lee, S. Zhou, R. Fu, J. Yang, W. Guo, H. Huang, J.-S. Lee, C. Wang, T. R. Kim, D. Nordlund, P. Pianetta, X. Du, J. Zhao, Y. Liu, J. Qiu, *Joule* **2020**, *4*, 673–687.
- [50] Y. Yang, X. Wang, F. Huang, J. Zhao, X. Wang, *Dalton Trans.* **2020**, *49*, 17310–17320.
- [51] Y. D. Miao, T. D. Wang, J. L. Hua, K. Y. Liu, Z. Y. Hu, Q. Li, M. Zhang, Y. X. Zhang, S. H. Liu, X. L. Xue, J. Q. Qi, F. X. Wei, Q. K. Meng, Y. J. Ren, B. Xiao, Y. W. Sui, P. Cao, *ACS Appl. Mater. Interfaces* **2021**, *13*, 39205–39214.
- [52] Y. X. Zhong, X. Y. Cao, Y. Liu, L. Cui, J. Q. Liu, *J. Colloid Interface Sci.* **2021**, *581*, 11–20.

Manuscript received: January 12, 2022

Revised manuscript received: February 22, 2022

Accepted manuscript online: February 25, 2022